

Mantle Phase Change Detection from Stochastic Tomography

Vernon F. Cormier¹, Yiteng tian², and Yingcai Zheng³

¹University of Connecticut

²University of Connecticut

³University of Houston

November 22, 2022

Abstract

Peaks are observed in a depth dependent power spectrum of P-wave velocity fluctuations determined from an inversion of P wave coherences observed by the USArray. These peaks correlate with the depths of the majority of silicate mineral phase changes predicted by a thermodynamic model of the upper 1000 km of a pyrolitic mantle. To within ± 25 km we identify the phase change of orthopyroxene to HP-clinopyroxene at 275 km, the olivine to wadsleyite phase change at 425 km, the wadsleyite to ringwoodite phase change at 505 km, and the initiation of an akimotoite phase at 600 km and a signature of a phase change at 775 km, both associated with the existence of fragments of subducted oceanic crust. Non-detection of a phase change at or near 660 is consistent with the phase change of ringwoodite to Mg-perovskite and magnesiowustite occurring over a depth interval much smaller than 25 km.

Mantle Phase Change Detection from Stochastic Tomography

Vernon F. Cormier¹, Yiteng Tian¹, and Yingcai Zheng²

¹Department of Physics, University of Connecticut

²Department of Earth and Atmospheric Sciences, University of Houston

Corresponding author: Vernon Cormier (vernon.cormier@uconn.edu)

†Vernon F. Cormier, Department of Physics, University of Connecticut, 196A Auditorium Road, Storrs, CT 06269-3046

Index terms: 7203, 7208, 7260, 3611, 3612

Key Points:

- An application of stochastic tomography exhibits peaks in depth in the inverted heterogeneity spectrum of the upper mantle.
- These peaks correlate with the majority of predicted mineral phase changes in the mantle.
- Phase change detection requires a dense seismic array and distributions of groups of earthquakes and estimates of their mechanisms.

22 **Abstract**

23 Peaks are observed in a depth dependent power spectrum of P-wave velocity fluctuations
24 determined from an inversion of P wave coherences observed by the USArray. These peaks
25 correlate with the depths of the majority of silicate mineral phase changes predicted by a
26 thermodynamic model of the upper 1000 km of a pyrolitic mantle. To within ± 25 km we
27 identify the phase change of orthopyroxene to HP-clinopyroxene at 275 km, the olivine to
28 wadsleyite phase change at 425 km, the wadsleyite to ringwoodite phase change at 505 km, and
29 the initiation of an akimotoite phase at 600 km and a signature of a phase change at 775 km, both
30 associated with the existence of fragments of subducted oceanic crust. Non-detection of a phase
31 change at or near 660 is consistent with the phase change of ringwoodite to Mg-perovskite and
32 magnesiowustite occurring over a depth interval much smaller than 25 km.

33 **Plain Language Summary**

34 Fluctuations in amplitude and traveltimes of seismic P waves from deep earthquakes observed at
35 the USArray of seismic stations are inverted for a depth dependent spectrum of the intensity P
36 wave velocity fluctuations. Peaks with depth of this spectrum correlate with the depths predicted
37 for changes in the arrangements of atoms of the silicate minerals comprising the upper 1000 km
38 of Earth's mantle.

39 **1 Introduction**

40 Modern reference Earth models typically have few first order discontinuities in the upper mantle.
41 These include commonly agreed ones at or near 400 and 660 km depth, which are interpreted to
42 be changes in solid phase of silicate minerals from the effect of increasing pressure with depth.
43 They are routinely observed in complex, double-triplicated, body waveforms between 15° to 35° ,
44 associated with near grazing incidence on two nearly discontinuous increases in P and S wave
45 velocities and densities at these depths. They are often also observed from partial reflections at
46 steeper angles of incidence from P to S conversions in receiver functions and in underside
47 reflections and conversions arriving as precursors to PP waves. In each of these observations the
48 detection of the sharp change in velocity and density depends on the width of the phase transition
49 in depth being narrower than the characteristic wavelength of the incident body wave.
50 Dziewonski & Anderson (1981) recognized early that the steep velocity gradients required to

51 exist in the mantle transition zone between the 400 and 660 discontinuities in PREM likely
52 masked a more complex set of mineral phase transitions occurring over broader intervals in
53 depth. In addition to those in the transition zone, the existences of other phase changes may
54 manifest themselves not as reflective discontinuities but rather as broader zones of increased
55 small-scale heterogeneity.

56

57 Small-scale heterogeneities, unresolvable by conventional tomography, have detectible
58 signatures in the fluctuation of amplitudes and travel times observed across seismic arrays.
59 Numerical simulations have shown that small-scale heterogeneity in the upper mantle can affect
60 the wavefront of an incident teleseismic wave beneath an array. Small differences in the angle of
61 approach of wavefronts, on the order of a several degrees or less, can produce unique signatures
62 in amplitude and phase fluctuations due to differences in the sensitivity of the wavefronts to the
63 small-scale structure (e.g., Zheng & Wu 2008; Tkalcic et al., 2010). Measurement of these
64 fluctuations between array elements can be exploited to invert for the spectrum of heterogeneity
65 beneath the array with techniques that have been named stochastic tomography (Wu & Flatté,
66 1990; Wu & Xie, 1991, Zheng & Wu, 2008).

67

68 Applying stochastic tomography to amplitude and phase fluctuations observed from three groups
69 of deep focus earthquakes by elements of the USArray, we inverted for a depth dependent
70 heterogeneity spectrum in the upper 1000 km beneath the western US (Cormier et al., 2020).
71 The inverted heterogeneity spectrum is characterized by a series of peaks that strongly correlate
72 with the depths of silicate phase changes predicted by thermodynamic models (Stixrude &
73 Lithgow-Bertelloni, 2007, 2012). The majority of these detected phase changes are expressed by
74 relatively weak changes in seismic velocity gradient spaced over a depth range on the order of or
75 larger than a wavelength, making them undetectable by high frequency, reflected and converted,
76 body waves.

77

78 In this paper, we interpret in detail the individual peaks in the heterogeneity spectrum we
79 published in a smoothed form, showing them in a raw, depth-discretized, form with error bars.
80 From these interpretations we estimate constraints on the depth and widths of the detected phase

81 transitions. We first briefly review the application of stochastic tomography in our previous
 82 paper (hereafter referred to as CICIP 2020). We conclude with a commentary on the experimental
 83 design needed to resolve peaks in the heterogeneity spectrum with depth. In conjunction with
 84 this paper we also provide downloadable Python and Matlab scripts to assist researchers in
 85 designing experiments with stochastic tomography (Tian and Cormier, 2020). These example
 86 scripts treat the effects of earthquake moment tensors and source-time functions on the reference
 87 wavefields defining coherence measurements.

88 **2 Methods and Application**

89 Transmission fluctuation coherence measurements (eqs. 1a-d) are the starting point for stochastic
 90 tomography. We consider the recorded fields due to two plane waves, PW1 and PW2. We use
 91 $U_1(x_1)$ for the recorded field at x_1 for PW1. Likewise, we use $U_2(x_2)$ for the recorded field at x_2
 92 for PW2. Both fields propagate through the same heterogeneous medium. We also consider their
 93 corresponding reference fields (no heterogeneities), $U_{1ref}(x_1)$ and $U_{2ref}(x_2)$, respectively. We
 94 can write the seismic fields in amplitude and phase terms, for example, $U_1 = u_1 \exp[i\omega t] =$
 95 $u_1 \exp[i\phi]$ and $U_{1ref} = u_{1ref} \exp[i\omega t_{ref}] = u_{1ref} \exp[i\phi_{ref}]$. Similar representations are
 96 applied to PW2. A Rytov approximation provides the relationship between the scattered field and
 97 the reference field: $U_1 = U_{1ref} e^{\Psi_1}$. The complex function Ψ has a real part, which is the
 98 logarithmic amplitude, and an imaginary part, which is the phase (or traveltime) difference. In
 99 our work, the observables are the ratios of log amplitude and travel time differences (eqs. 1c-d)
 100 from those computed in a reference Earth model. Transverse coherence functions are
 101 constructed as a function of the lag distance x between pairs of receivers. The brace brackets in
 102 eqs. 1a-b, define the logarithmic amplitude $\langle u_1 u_2 \rangle$ and $\langle \phi_1 \phi_2 \rangle$ phase coherences by averaging
 103 measurements for a specific lag distance over all combinations of two receivers in an array
 104 separated by that lag distance. Non-dimensional coherence values range from zero (no
 105 correlation in signal amplitude and traveltime fluctuations) at neighboring receivers to 1 for
 106 perfect correlation.

107

$$(1a) \quad \langle u_1 u_2 \rangle = \frac{1}{2} \text{Re} \langle \psi_1 \psi_2^* \rangle + \frac{1}{2} \text{Re} \langle \psi_1 \psi_2 \rangle$$

$$(1b) \quad \langle \phi_1 \phi_2 \rangle = \frac{1}{2} \text{Re} \langle \psi_1 \psi_2^* \rangle - \frac{1}{2} \text{Re} \langle \psi_1 \psi_2 \rangle, \quad \text{where}$$

$$(1c) \quad \hat{\psi}(\omega) = \ln(u / u_{ref}) + i\omega(t - t_{ref})$$

$$(1d) \quad u = \frac{\psi + \psi^*}{2} \quad \text{and} \quad \phi = \frac{\psi - \psi^*}{2}$$

108

109

110 To construct the complex functions $\hat{\psi}(\omega)$, we measure u and u_{ref} from observed and synthetic
111 seismograms around the direct P waves from the outputs of a multi-taper filter at 0.7 Hz, and
112 measure the traveltime difference

113 $t - t_{ref}$ from cross-correlation of observed and predicted reference waveforms.

114

115 Stochastic tomography assumes that the functional behaviors of the coherences with lag distance
116 are due to the interference of plane waves scattered by heterogeneity having an unknown power
117 spectrum as a function of wavenumber and depth. The transverse coherences can be written as
118 an integral over horizontal wavenumber and depth, with an integrand containing the power
119 spectrum (eqs. 2a-c).

120

$$(2a) \quad \langle u_1 u_2 \rangle = (2\pi)^{-1} \int_0^H d\xi a_1(\xi) a_2(\xi) \int_0^\infty J_0[(\kappa R(\xi))] \sin[\omega\theta_1(\xi)] \sin[\omega\theta_2(\xi)] P(\xi, \kappa) \kappa d\kappa$$

$$(2b) \quad \langle \phi_1 \phi_2 \rangle = (2\pi)^{-1} \int_0^H d\xi a_1(\xi) a_2(\xi) \int_0^\infty J_0[(\kappa R(\xi))] \cos[\omega\theta_1(\xi)] \cos[\omega\theta_2(\xi)] P(\xi, \kappa) \kappa d\kappa$$

$$(2c) \quad \langle u_1 \phi_2 \rangle = (2\pi)^{-1} \int_0^H d\xi a_1(\xi) a_2(\xi) \int_0^\infty J_0[(\kappa R(\xi))] \sin[\omega\theta_1(\xi)] \cos[\omega\theta_2(\xi)] P(\xi, \kappa) \kappa d\kappa$$

122

123 In eqs. 2a-c, P is the power spectrum as a function of depth ξ and horizontal wavenumber κ .

124 H is the thickness of a heterogeneous layer. Functions a_1, a_2, θ_1 , and θ_2 are defined in CICP

125 2020. The function R appearing in the argument of the Bessel function J_0 is the horizontal

126 distance between the pair of rays arriving at a specific lag distance at depth ξ . The average sum

127 of a coherence measurement at each lag from many sources at different distances and azimuths

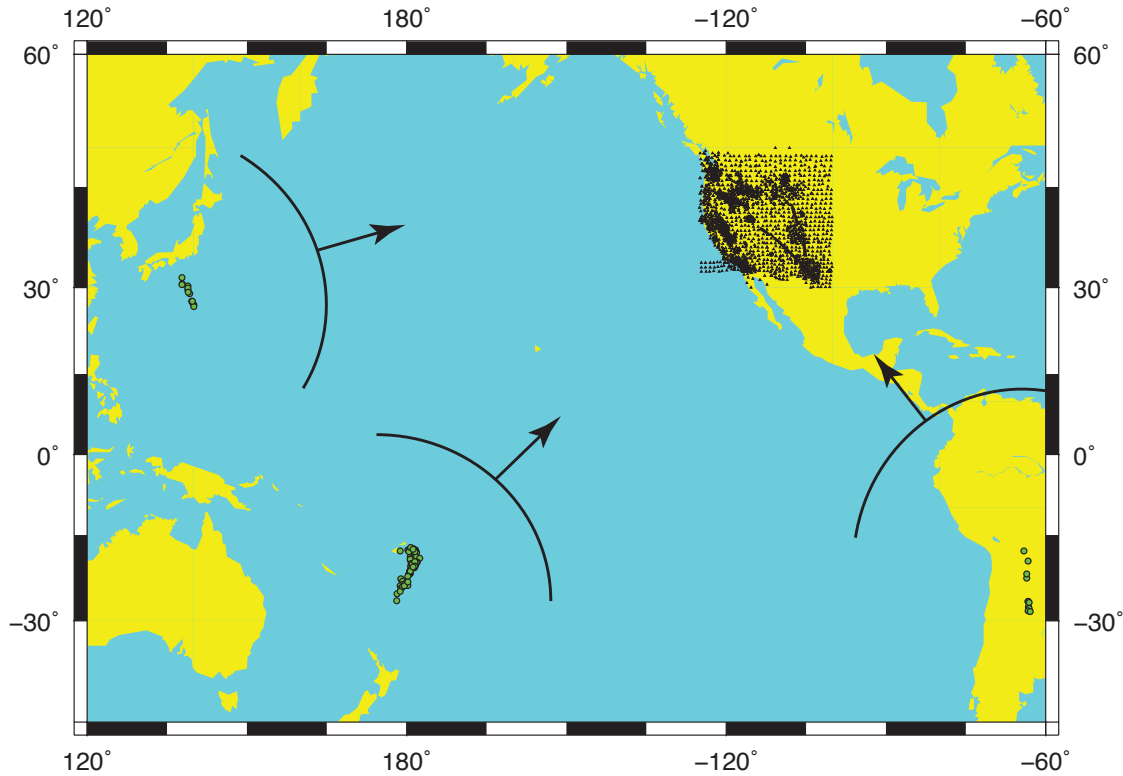
128 can, in principle, be sensitive to the effects of scatterers whose size may be less than the spacing
129 of array elements.

130

131 These integrals can be discretized and set-up as a linearized inverse problem in which the
132 squared difference of the observed coherences and predicted coherences of an unknown power
133 spectrum are minimized. The discretized forms of eqs.2a-c and the object function to be
134 minimized are given in Appendix B of CICP 2020.

135

136 In CICP 2020 the coherence data we chose to invert were 3 groups of deep focus earthquakes
137 (Marianas, Tonga-Kermadec, and South America) observed by elements of the US array and
138 transportable array in the western US (Fig. 1). Deep focus events were chosen to avoid the
139 effects of heterogeneity concentrated in the upper mantle near the source and to eliminate the
140 effects of near source reflections. P waveforms of 21,205 deep focus earthquakes having moment
141 magnitudes M_w between 5.8 to 6.2 were downloaded from the Data Management Center of
142 IRIS. About 40% of these had sufficiently high signal to noise ratios and simple apparent
143 source-time functions to include in the coherence measurements. Within each earthquake group,
144 measured coherences are averaged at all receiver pairs corresponding to a specific lag.
145 Wavefront healing due to propagation from the source to the teleseismic receivers as well as
146 coherence over earthquakes aids in eliminating any source-side heterogeneity effects. A joint
147 inversion of data comprising 3 wavefronts arriving from widely different azimuths, whose rays
148 cross at variable depths beneath the array, makes it possible to achieve a sensitivity to
149 heterogeneity scales slightly smaller than the spacing of array elements.



150

151

152 **Figure 1.** Hypocenters of three deep-focus earthquake groups and US Array seismic stations
 153 used in the inversion of P wave coherence for the upper mantle heterogeneity spectrum.

154

155 The inclusion of the effects of the specific earthquake source-time functions and radiation
 156 patterns in u_{ref} are essential to isolating the effects of forward scattering from those of the source.

157 To achieve this for each event the reference synthetic seismogram u_{ref} at each array element was

158 computed from the IRIS Syngine service (Nissen-Meyer, et al., 2014;

159 <https://service.iris.edu/irisws/syngine>) in the AK135-F Earth model (Montagner & Kennett,

160 1995) using the known moment tensor solution for each event from the GCMT service (Ekstrom

161 et al., 2012; <https://www.globalcmt.org>) and an empirical source time function determined by

162 stacking P waves from each event in the 40° to 90° distance range.

163

164

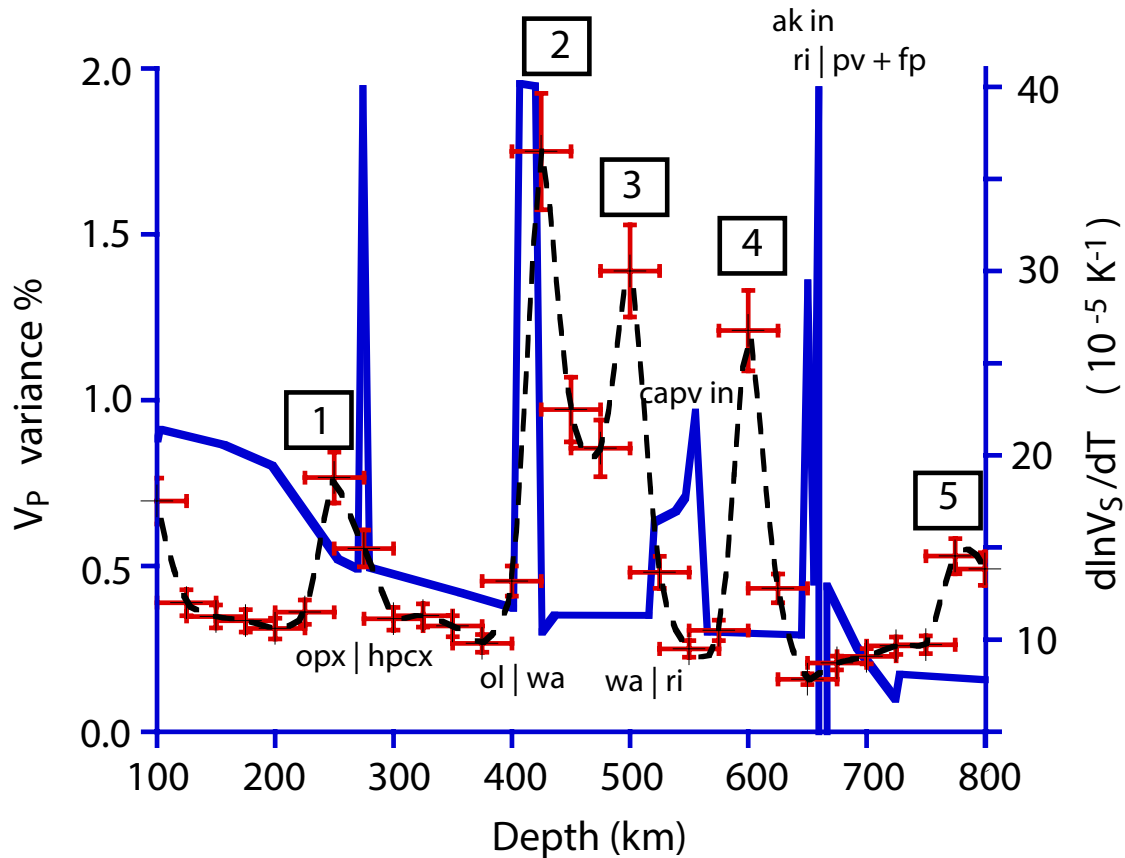
165 We first inverted for a constant heterogeneity spectrum with depth in which the shape of the
166 power spectrum was defined by 4 parameters. We then assumed that the spectral shape in
167 wavenumber determined from the single layer inversion was constant in depth but allowed its
168 peak power to vary with depth in 40, 25 km thick, layers. Comparing the depth dependent
169 inversion to the single layer inversion, the squared coefficient of determination increased from
170 0.74 to 0.80 and the reduced χ^2 decreased from 1.65 to 1.05. The significantly smaller, but not
171 less than 1, χ^2 for the depth dependent spectrum is consistent with an improved fit, but not an
172 over- fit due to the assumption of a larger number of unknown parameters. Plots of our observed
173 and predicted coherences from both types of inversions are shown in CICP 2020.

174

175 **3 Results**

176 **3.1 Interpretation of the depth dependent heterogeneity spectrum**

177 Results of our inversion for a depth dependent heterogeneity spectrum for the upper 1000 km of
178 the mantle beneath the western US for the root-mean-square (rms) P velocity fluctuations are
179 shown in Fig. 2. The complexity of the spectrum with depth, consisting of narrow peaks, does
180 not resemble a smooth 1-D depth spectrum, with power decaying with depth in the upper mantle,
181 commonly resolved in conventional travel time tomography. The error bars in depth in Fig. 2 are
182 fixed at 25 km to equal the sampling rate for the 40 depth values used in our inversion. The
183 ordinate error bars in the power of rms velocity fluctuation are taken to be 10% of the ordinate
184 value. To our surprise the depth of the peaks correlate well with ones that have been predicted in
185 a thermodynamic model of mantle heterogeneity by Stixrude & Lithgow-Bertelloni (2007). This
186 model assumes a pyrolitic composition in which chemistry and phase vary with depth to achieve
187 an equilibrium state that minimizes Gibbs free energy. The effective temperature derivative of
188 shear velocity for this model shown in Fig. 2 assumes an adiabatic temperature gradient and a
189 1600° K potential temperature. In related models, Stixrude & Lithgow-Bertelloni (2012)
190 demonstrate the effects of varying potential temperature and mechanical mixing of harzburgite
191 and basalt to simulate the effects of slab cycling.



192

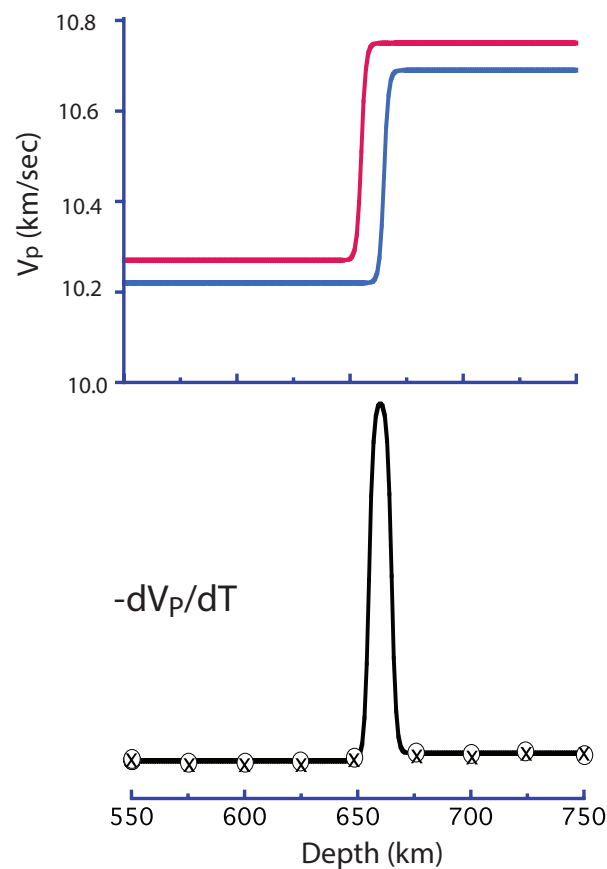
193 **Figure 2.** The depth dependent heterogeneity spectrum for the rms fluctuation of P wave
 194 velocity in the upper 1000 km of the mantle compared with the temperature derivative of shear
 195 velocity predicted in the thermodynamic pyrolitic model in Stixrude & Lithgow-Bertelloni
 196 (2007). Numbered silicate mineral phase changes next to peaks in the temperature derivative are
 197 keyed to interpretations in this section.

198

199

200 Predicted peaks in the temperature derivative of seismic velocities are from metamorphic
 201 contributions due to phase and chemistry changes (Fig. 3). The expression of these changes in
 202 seismic velocity can either be sharp or spread out over a depth range bounded by two changes in
 203 the gradient of seismic velocity. If sharp, the phase change can be detectable from reflected,
 204 converted, or multipathed body waves, and the effect of lateral temperature variations will be
 205 expressed as topography on an apparent seismic reflector. If spread out over a depth range, the
 206 phase change will not be detectable in seismic reflections or receiver function processing, but
 207 will be detectable as discrete scatterers in a narrow range of depth. In this case, the horizontal

208 length scale of the scatterers will be related to the lateral scale of temperature variations and the
209 vertical scale to the width of the depth (pressure) range over which the phase change occurs. It is
210 just this type of phase change that can be detectable by stochastic tomography, which seeks to
211 image stochastically described forward scattering with depth. Note in Fig.3 that the depth
212 sampling of estimated scattering power may not be able to detect phase changes that occur over a
213 depth interval shorter than the sampling rate.
214



215

216

217 **Figure 3.** Top: the effect of a temperature variation on the P velocity due to an endothermic
218 phase change near 660 km depth (red hotter/blue colder) Bottom: the metamorphic contribution
219 to the temperature derivative of P velocity computed by a difference derivative. Crosses are at

220 the 25 km depth-sampling interval of the heterogeneity spectrum derived from the stochastic
221 tomography inversion.

222

223 Keeping these factors and limitations in mind, we can begin to interpret the correlations in Fig. 2
224 between the predicted peaks in the temperature derivative of seismic velocity from the
225 thermodynamic mantle model and the peaks in depth of the heterogeneity power determined
226 from stochastic tomography. A possible interpretation of the correlations follows:

227

228 (1) A peak at 250 ± 25 km correlates with a predicted phase change of orthopyroxene to HP-
229 clinopyroxene at 275 km.

230 (2) A peak at 425 ± 25 km correlates with a predicted phase change of olivine to wadsleyite
231 between 405 to 418 km.

232 (3) A peak at 500 ± 25 km correlates with a predicted phase change of wadsleyite to
233 ringwoodite at 505 km. The predicted signal in the temperature derivative of velocity,
234 however, consists of a relatively wide peak in which the shallower wadsleyite to
235 ringwoodite phase change interferes with an initiation of a deeper calcium perovskite
236 phase (capv in) at 545 km.

237 (4) A peak at 600 ± 25 km nearly correlates with two predicted interfering phase changes: an
238 exothermic phase change with the initiation of akimotoite (ak in) having a positive
239 temperature derivative of velocity, followed by predicted endothermic phase change from
240 ringwoodite to perovskite and ferropericlasite (ri to pv + fp). In the thermodynamic model
241 these two interfering phase changes occur between 650 to 660 km depth.

242 (5) A peak at 775 ± 25 km correlates with one predicted at 785 km in mechanical mixtures of
243 basalt and harzburgite having a basalt fraction of 18%, indicative of a phase change in
244 subducted oceanic crust.

245

246 The differences between detected and predicted phase changes will depend on the accuracy of
247 the assumptions in the thermodynamic model and the sampling and errors in the power spectrum
248 of heterogeneity determined from stochastic tomography. The depth accuracy of the
249 thermodynamic model depends on the validity of the assumed petrologic model and the physical
250 properties of minerals determined from combinations of experimental observations and ab initio

251 calculations. The depth accuracy of the power spectrum largely depends on the depth-sampling
252 rate that can be resolved in the inversion of coherences, which depends on sensor spacing and its
253 geometry and the azimuthal and depth distribution of seismic events.

254
255 For the 25 km depth sampling possible in this study, some general conclusions can be made
256 about the achievable accuracy for stochastic tomography applied to the US Array. Except for a
257 disagreement between an observed and predicted 660 km seismic discontinuity, the depths of the
258 majority of predicted and observed phase changes agree within estimated errors. This suggests
259 that a pyrolitic thermodynamic model having a 1600° potential temperature and some
260 mechanical mixing of subducted basalt is an adequate model for the upper 1000 km beneath the
261 western US. The depth of nearly all other predicted phase changes has been detected within
262 estimated error of +/- 25 km, suggesting that the transition width of at least some of these phase
263 changes may equal or exceed 25 km.

264
265 The disagreement between the detected (600 km) and predicted (660 km), last and deepest, major
266 phase change is too large to be explained by a plausible hotter mantle temperature in this broad
267 region. A global 660 km discontinuity has been largely confirmed in many seismic studies and
268 is generally the most robustly detected discontinuity even by reflected body waves having
269 dominant frequencies approaching 1 Hz (e.g., Deuss et al., 2006). Its signature in receiver
270 functions (Andrews & Deuss, 2006), however, can be complex, in agreement with the complex
271 phase changes predicted from thermodynamic models at and near this depth (Xu et al., 2008). A
272 partial explanation for a positive detection at 600 km but not 660 km is that the 25 km sampling
273 rate in the inversion is simply too coarse to resolve the complex signal of two closely spaced
274 phase changes. In addition, the positive detection at 600 km may instead be a detection of the
275 predicted transformation of high-pressure clinopyroxene to akimotoite initiating closer to 600
276 rather than 650 km (Hao et al., 2019), having a transition width in depth on the order of 25 km or
277 greater. The predicted phase change at 660 km of ringwoodite to Mg-perovskite and
278 magnesiowustite, estimated to have a transition width of 2 km (Ishii et al, 2019), may be more
279 easily detectable from reflected and converted body waves than from a stochastic power
280 spectrum having a sampling interval of 25 km.

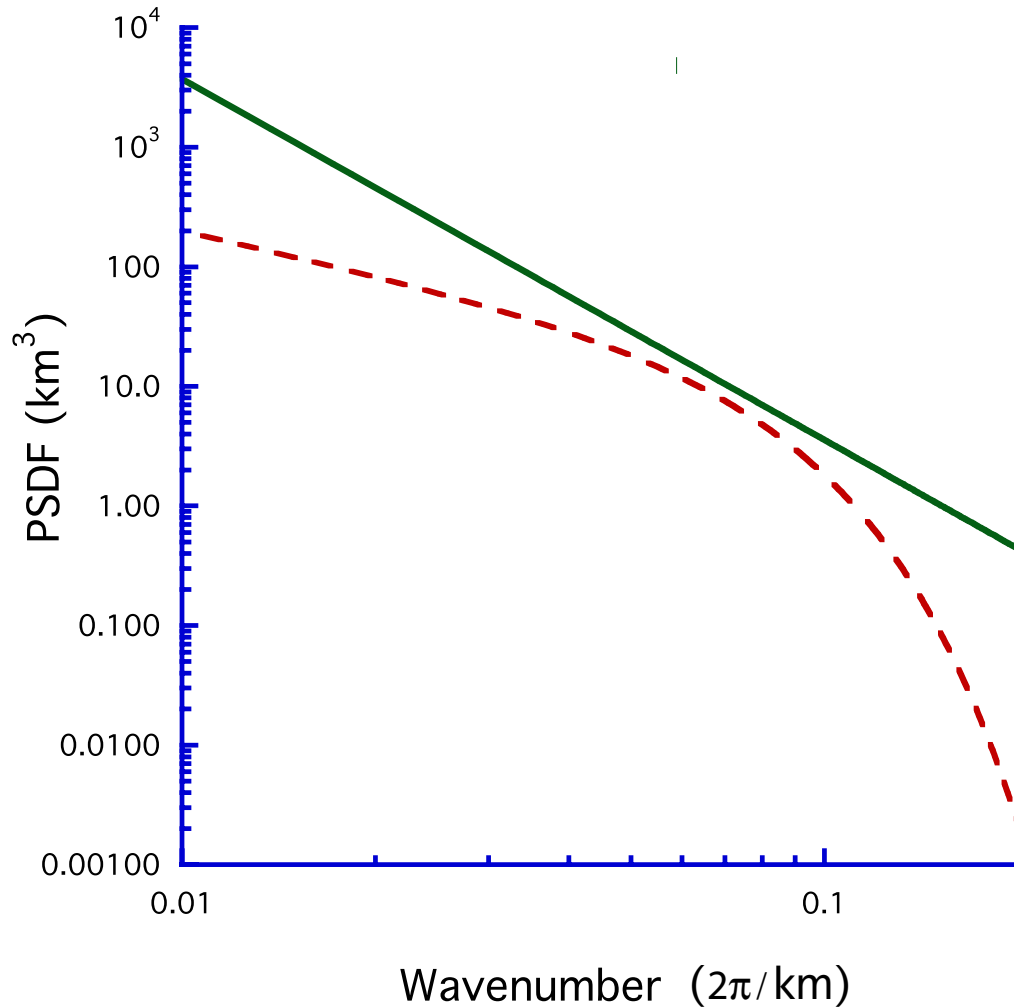
281

282 The detection of an akimotoite transition at 600 km, indicative of the existence of regions of
283 colder mantle temperatures (Hogrefe et al., 1994), coupled with a phase transition at 775 km, is
284 consistent with the history of the subduction of the Farallon plate beneath the western US.
285 Tomographic images of the shear velocity structure of the mantle beneath this region reveal
286 evidence of both slab stagnation and fragmentation in the lower mantle transition zone as well as
287 penetration beneath 660 km (Schmid et al., 2002).

288

289 **3.2 Comparison with non-depth dependent heterogeneity spectra**

290 It is useful to factor out the wavenumber dependence from our depth dependent spectrum and
291 compare its spectrum against other non-depth dependent, stochastic models of upper mantle
292 heterogeneity. In the context of understanding how lateral temperature differences drive mantle
293 heterogeneity such a comparison can provide some constraints on the compositional and
294 temperature variations in the upper mantle at scale lengths intermediate between those estimated
295 from global travel-time tomography and the coda of high-frequency body waves.



296

297 **Figure 4.** Mancinelli et al.'s (2016) heterogeneity spectrum (solid green line) compared with our
 298 single layer (dashed red line), isotropic heterogeneity spectrum.

299

300 Mancinelli et al. estimated a 1-D von Karman spectrum for the upper mantle based on the
 301 scattered coda of broadband body waves and the power spectrum of larger scale heterogeneity
 302 resolved by global tomography. Our inverted heterogeneity spectrum was a 3-D isotropic
 303 spectrum. Hence, to make the comparison shown in Fig. 4, we converted the 1-D spectrum in
 304 Mancinelli et al. to a 3-D isotropic spectrum for a von Karman medium using formulas in Sato et
 305 al. (2012). Our spectrum was parameterized by shape parameters recommended by Klimes
 306 (2002), consisting of a product of a low pass and high pass filter in wavenumber. We chose this
 307 type of parameterization to recognize that the sensitivity of our coherence data peaked around a
 308 narrow band in wavenumber. In contrast, the data fit by Mancinelli et al. weight the effects of

309 heterogeneity over a much broader band of wavenumber, corresponding to frequencies from
310 millihertz to 10 Hz. The two spectra nearly coincide in a narrow wavenumber band centered near
311 0.065 km^{-1} . From the region of match in wavenumber, we conclude that scale length of
312 heterogeneities induced by lateral variations in upper mantle phase transitions has a lateral scale
313 length on the order of 100 km. This suggests that our coherence measurements reveal the
314 existence of a significant lateral scale on the order of 100 km for variations in chemistry,
315 temperature (100° to 500° K), or both.

316 **4 Conclusions**

317 The application of stochastic tomography to invert for a depth dependent heterogeneity spectrum
318 in the upper 1000 km of the mantle reveals a strong correlation with the majority of predicted
319 phase changes from a thermodynamic model of a pyrolitic mantle. This demonstrates that
320 stochastic tomography has the potential to detect mantle phase changes that do not exhibit
321 changes in seismic velocity and density over short depth intervals. These types of phase changes
322 are characterized by paired changes in velocity gradient over a transition depth that may be equal
323 to or larger than the wavelength of a body wave.

324

325 Results from a depth-sampling interval of 25 km for the inverted spectrum for the upper mantle
326 beneath western North America suggest that many of these phase changes may occur over a
327 range in depth equal to or greater than 25 km. An exception is our non-detection of the phase
328 transition at 660 km, consistent with a transition interval in depth that may be as small as 2 km
329 (0.1 GPa).

330

331 To detect changes in mantle phases with stochastic tomography requires not only a depth-
332 sampling interval on the order of 25 km or less, but also estimation of the amplitude and phase
333 effects of source radiation patterns and source-time functions. Resolution will also be improved
334 by averaging of measured coherences at each lag over a large number of earthquakes arriving
335 from sufficiently different azimuths. The 40 km spacing of the US Array elements and the
336 availability of waveforms from 3 widely separated groups of deep focus earthquakes, having
337 simple source-time functions, makes this possible for at least the western US. Similar to the
338 1970's discovery of the 400 and 660 km mantle velocity discontinuities (Burdick & Helmberger,

339 1978), which required the incorporation of the effects of earthquake sources, the detection of less
340 pronounced mantle phase changes, will generally require routine source-time function and
341 moment tensor estimation.

342 **Acknowledgments and Data**

343 This study was supported by the National Science Foundation under grant EAR 14-46509
344 (Vernon Cormier and Yiteng Tian) and grant EAR 16-21878 (Yingcai Zheng). Interpretations
345 benefited from discussions with Lars Stixrude, Carolina Lithgow-Bertelloni, and Hao Hu. Figure
346 1 was drawn using the Generic Mapping Tools (Wessel and Smith, 1998).

347

348 Waveform data and services for centroid moment tensors and synthetic seismograms are
349 available from the Incorporated Research Institutions for Seismology through the web site
350 <https://www.iris.edu>. Matlab and Python scripts for processing and inverting amplitude and
351 phase coherences for single layer and depth dependent heterogeneity spectra are available for
352 download from the sites in the Tian & Cormier (2020) entry in the References.

353

354 **References**

355 Andrews, J., and Deuss, A. (2008), Detailed nature of the 660 km region of the mantle from
356 global receiver function data. *J. Geophys. Res.*, 113 (B6). doi:10.1029/2007JB005111.

357

358 Burdick, L.J., and Helmberger, D.V. (1978), The upper mantle P velocity structure of the
359 western United States. *J. Geophys. Res.*, 83 (B4), 1699-1712.

360

361 Cormier, V.F., Tian, Y., & Zheng, Y. (2020), Heterogeneity spectrum of Earth's upper mantle
362 obtained from the coherence of teleseismic P waves. *Commun. Comp. Phys.*, 28, 74-97. doi:
363 10.4208/cicp.OA-2018-0079.

364

365 Deuss., A., Redfern, S.A.T., Chambers, K., & Woodhouse, J.H. (2006), The nature of the 660
366 km discontinuity in Earth's mantle from global seismic observations of PP precursors. *Science*,
367 311, 198-201.

- 368
369 Dziewonski, A.M., & Anderson, D.L., (1981), Preliminary Reference Earth Model. *Phys. Earth*
370 *Planet. Int.*, 25 (4), 297-356.
- 371
372 Ekstrom, G., Nettles, M., & Dziewoski, A. M., (2012), The global CMT project 2004-2010:
373 Centroid moment tensors for 13,017 earthquakes. *Phys. Earth Planet. Int.*, 200-201, 1-9, doi:
374 10.1016/j.pepi.2012.04.002.
- 375
376 Hao, S., Wang, W., Qian, W., & Wu, Z. (2019), Elasticity of akimotoite under the mantle
377 conditions: Implications for multiple discontinuities and seismic anisotropies at the depth ~600-
378 750 km in subduction zones. *Earth Planet. Sci. Lett.*, 528, 115830.
- 379
380 Hogrefe, A., Rubie, D.C., Sharp, T.G., (1994), Metastability of enstatite in deep subducting
381 lithosphere. *Nature*, 372 351-353.
- 382
383 Ishii, T., Huang, T., Myhill, R., Fei, H. Koemets, L., Liu, Z., Maeda, F., Yuan, L., Wang, L.,
384 Druzhbin, D., Yamamoto, T., Bhat, S., Faria, R., Kawazoe, T., Tsujino, N., Kulik, E., Higo, Y.,
385 Tange, Y., & Katsura, T. (2019), Sharp 660-km discontinuity controlled by extremely narrow
386 binary post-spinel transition. *Nature Geoscience*, 12, 869-872.
- 387
388 Klimes, K. (2002), Correlation functions of random media. *Pure Appl. Geophys.*, 159 1811-
389 1831.
- 390
391 Mancinelli, N., and Shearer, P., Liu, Q. (2016), Constraints on the heterogeneity spectrum of
392 Earth's upper mantle. *J. Geophys. Res.*, 121 (5), 3703-3721.
- 393
394 Montagner, J.P., and Kennett, B.L.N., (1995), How to reconcile body-wave and normal-mode
395 reference Earth models? *Geophys. J. Int.*, 135-229-248.
- 396
397 Nissen-Meyer, T., van Driel, M., Stähler, S. C., Hosseini, K., Hempel, S., Auer, L., Colombi, A.,
398 & Fournier, A. (2014) AxiSEM: broadband 3-D seismic wavefields in axisymmetric media.

- 399 *Solid Earth*, 5, 425-445, <https://doi.org/10.5194/se-5-425-2014>.
400
- 401 Sato, H., Fehler, M.C., & Maeda, T. (2012), *Seismic Wave Propagation and Scattering in the*
402 *Heterogeneous Earth*, 2nd edn., Springer-Verlag.
403
- 404 Schmid, C., Goes, S., van der Lee, S., & Giardini, D. (2002), Fate of the Cenozoic Farallon slab
405 from comparison of kinematic thermal modeling with tomographic images. *Earth and Planet.*
406 *Sci. Lett.*, 204, 17-32.
407
- 408 Stixrude, R., & Lithgow-Bertelloni, C. (2007), Influence of phase transformations on lateral
409 dynamics in Earth's mantle. *Earth Planet. Sci. Lett.*, 263, 45-55.
410
- 411 Stixrude, R., & Lithgow-Bertelloni, C. (2012), Geophysics of chemical heterogeneity in the
412 mantle. *Ann. Rev. Earth Planet. Sci.*, 40, 569-595.
413
- 414 Tian, Y., & Cormier, V.F., (2020), https://github.com/vernoncormier/stochastic_tomography,
415 doi:10.528/zenodo.4000538.
416
- 417 Tkalčić, H., Cormier, V.F., Kennett, B.L.N., & He, K. (2010), Steep reflections from the Earth's
418 core reveal small-scale heterogeneity in the upper mantle. *Phys. Earth Planet. Int.*, 178, 80-91.
419 doi: 10.1016/j.pepi.2009.08.004.
420
- 421 Wessel, P., and Smith, W.H.F. (1998), New, improved version of the Generic Mapping Tools
422 released, *Eos Trans. AGU*, 79, 579.
423
- 424 Wu, R.S., & Flatté, S. (1990), Transmission fluctuations across an array and heterogeneities in
425 the crust and upper mantle. *Pure Appl. Geophys.*, 132, 175-196.
426
- 427 Wu, R.S., & Xie, X. (1991), Numerical tests of stochastic tomography. *Phys. Earth Planet.*
428 *Inter.*, 67 (1991) 180-193.
429

430 Xu, W., Lithgow-Bertelloni, C., Stixurde, L., and Ritsema, J. (2008), The effect of bulk
431 composition and temperature on mantle seismic structure. *Earth. Planet. Sci. Lett.*, 275, 70-79.

432

433 Zheng, Y., Wu, R.-S., (2008), Theory of transmission fluctuations in random media with
434 a depth dependent background velocity structure. *Adv. Geophys.*, 50, 21-41.

435

436

437

438

439

440

441

442

443

444

445